First-Principles Study of the Structural, Optical, Electronic and Strain-Dependent Properties of Caesium Bismuth Halide $Cs_3Bi_2X_9$ (X = I, Br, Cl) for Photovoltaic Applications

Uzma Aleeya Saiful Nizam[1], Fadhlul Wafi Badrudin[2], Shahrul Izwan Ahmad[2] and Nor Azlian Abdul Manaf[2]*

[1]Faculty of Defence Science & Technology, National Defence University of Malaysia, Kem Perdana Sg. Besi, 57000 Kuala Lumpur, Malaysia

[2]Physics Department, Centre for Defence Foundation Studies, 6th Floor, Bestari Building, National Defence University of Malaysia, Kem Perdana Sg. Besi, 57000 Kuala Lumpur, Malaysia

*Corresponding author (e-mail: azlian@upnm.edu.my)

In recent years, increasing environmental and stability concerns surrounding lead-based perovskites have driven extensive research toward the development of lead-free alternatives. Among the promising candidates, caesium bismuth halides ($Cs_3Bi_2X_9$, X = I, Br, Cl) have attracted significant attention due to their excellent chemical stability, favourable electronic properties, and tuneable band gap energies. In this work, a comprehensive density functional theory (DFT) study was conducted within the CASTEP framework to investigate the structural, optical, electronic, and mechanical strain-dependent properties of $Cs_3Bi_2I_9$, $Cs_3Bi_2Br_9$, and $Cs_3Bi_2Cl_9$. The optimized crystal structures confirmed their hexagonal and trigonal layered phases with stable lattice configurations. Optical absorption spectra revealed strong absorptions with coefficients on the order of 10^5 cm^{-1}, with the absorption edge systematically shifting towards shorter wavelengths from $Cs_3Bi_2I_9$ to $Cs_3Bi_2Br_9$ to $Cs_3Bi_2Cl_9$, corresponding to increasing band gap values. The calculated indirect band gaps were 1.96 eV ($Cs_3Bi_2I_9$), 2.46 eV ($Cs_3Bi_2Br_9$), and 3.05 eV ($Cs_3Bi_2Cl_9$). Under mechanical strain (±5 %), $Cs_3Bi_2I_9$ exhibited significant band gap tunability, increasing to 2.39 eV (+5 %) and 2.37 eV (−5 %), whereas $Cs_3Bi_2Br_9$ showed moderate reductions with 2.43 eV (+5 %) and 2.20 eV (-5 %), and $Cs_3Bi_2Cl_9$ with 3.00 eV (+5 %) and 2.98 eV (-5 %). These findings suggest that strain engineering effectively modulated the optoelectronic response, particularly in iodine-based compounds. Overall, this study provides valuable insights into the intrinsic and strain-dependent properties of $Cs_3Bi_2X_9$ perovskites and underscores their potential as sustainable, lead-free materials for next-generation photovoltaic and optoelectronic applications.

Keywords: $Cs_3Bi_2I_9$, $Cs_3Bi_2Br_9$, $Cs_3Bi_2Cl_9$, lead-free perovskite, CASTEP

Received: November 2025; Accepted: March 2026

The emergence of perovskite materials has revolutionised the field of photovoltaics, primarily due to their exceptional optoelectronic properties, cost-effective fabrication, and high-power conversion efficiencies (PCEs) exceeding 25 % in just over a decade [1-3]. However, most high-efficiency perovskite solar cells (PSCs) are based on lead-containing compounds such as methylammonium lead iodide ($MAPbI_3$) and formamidinium lead iodide ($FAPbI_3$) [4-5], raising serious concerns about their long-term environmental impact and stability. These concerns are substantiated by biological studies; for instance, exposure to dissolved $MAPbI_3$ has been shown to cause massive apoptotic death in primary hippocampal neurons and dramatically alter proliferation and metabolism in lung epithelial cells in vitro [6].

To address these challenges, researchers have increasingly focused on lead-free perovskite alternatives such as BiOI, $FASnI_3$, $CsSnI_3$. One of the most promising classes of lead-free perovskite materials is caesium bismuth halide perovskites ($Cs_3Bi_2X_9$, X = halide ions) [7-8]. These compounds have gained significant attention due to their excellent chemical stability, low toxicity, and structural similarity to conventional lead-based perovskites [9][10]. Halide perovskite materials constitute a revolutionary class of semiconductors, defined by the general formula AMX_3, where A is a monovalent cation (e.g., $CH_3NH_3^+$ (MA^+), $HC(NH_2)_2^+$ (FA^+), or Cs^+), M is a divalent metal cation (e.g., Pb^{2+} or Sn^{2+}), and X is a halide anion (I^-, Br^-, Cl^-) [11][12]. These materials typically crystallize in a three-dimensional structure characterized by a network of corner-sharing MX_6 octahedra, with the A-site cation occupying the cuboctahedral cavities to maintain charge neutrality. This versatile framework allows for extensive compositional tuning and exploration of diverse chemical and structural properties.

In addition, bismuth-based halide perovskites offer superior environmental compatibility and enhanced moisture resistance compared to other lead-free alternatives such as tin- or germanium-based perovskites, which often suffer from oxidation and instability issues [13]. Recent research has highlighted that low-dimensional halide perovskites exhibit superior carrier dynamics and robust exciton binding energies due to quantum confinement effects [14]. These properties make them excellent candidates for a range of applications, including light-emitting diodes, solar cells, and photodetectors, positioning them to revolutionize the optoelectronic field [15]. Among the halides (the X used in $Cs_3Bi_2X_9$) iodide, bromide and chloride counterparts demonstrate tuneable band gaps and adjustable optoelectronic properties through halide substitution, making them highly suitable for photovoltaic and optoelectronic applications [16-17]. $Cs_3Bi_2I_9$ possesses a high light absorption coefficient to absorb sunlight efficiently [18]. Meanwhile, $Cs_3Bi_2I_9$ features a layered structure formed by $[Bi_2I_9]^{3-}$ bioctahedra and Cs^+ ions, exhibiting an indirect band gap of ~2.0–2.2 eV. While this band gap is larger than the optimal value for single-junction cells and contributes to its historically modest efficiency, recent simulation studies have demonstrated its exceptional promise for tandem applications. Specifically, a standalone $Cs_3Bi_2I_9$ cell achieved a simulated efficiency of 20.37 %, and, more importantly, a four-terminal tandem with crystalline silicon yielded a remarkable 31.59 % efficiency, effectively leveraging its wide band gap to surpass the Shockley-Queisser limit [19].

To fully harness this potential for tandem applications, research has focused on optimizing the optoelectronic properties of $Cs_3Bi_2I_9$. Strategies such as halide substitution (replacing I^- with Br^- or Cl^-) and other doping approaches are being explored to fine-tune its band structure, enhance charge transport, and potentially engineer a more direct band gap, all critical factors for maximizing the performance of the wide-band gap top cell in a tandem architecture [8, 20-22].

Density Functional Theory (DFT) is a powerful computational approach commonly used to understand atomic-level effects. By leveraging quantum mechanical principles, DFT allows researchers to predict the structural, electronic, and optical properties of materials with high accuracy, offering insights that are often inaccessible through experiments alone [23]. Its benefits include relatively lower computational costs, reliable predictions of band structures and density of states, and the capability to model how dopants or defects influence material performance. This is exemplified in studies of perovskite oxides, such as a first-principles investigation into Cu-doped $SrTiO_3$, which revealed that Cu incorporation could favourably transform the material's band structure from an indirect to a direct gap by introducing new electronic states, a critical property for tailoring optoelectronic properties [24].

Mechanical strain has emerged as a powerful and widely explored strategy for tuning the physicochemical properties of semiconductor materials, particularly in soft halide perovskites. In halide perovskites, even a slight deformation can distort the metal–halide framework, altering bond lengths, orbital overlap, and ultimately modulating the electronic band structure. As these materials are mechanically soft and ionically bonded, strain can significantly affect defect populations, phase stability, and optoelectronic performance. Recent reviews highlight that strain is a key factor limiting device stability, but also a potential tool to engineer improved performance [15, 25]. For bismuth-based perovskites such as $Cs_3Bi_2X_9$, strain-dependent studies are particularly important: their relatively wide band gaps and moderate carrier mobility limit efficiency, and strain offers a non-chemical, reversible route to potentially narrow the band gap, enhance carrier transport, or stabilize favourable phases.

This work is a first-principles study based on density functional theory (DFT) calculations with the CASTEP software package to systematically investigate the structural, optical, electronic and mechanical properties of $Cs_3Bi_2I_9$, $Cs_3Bi_2Br_9$, and $Cs_3Bi_2Cl_9$. We analyze the band structure, density of states (DOS), and optical absorption spectra to assess their suitability and possible modifications for future photovoltaic applications.

METHODOLOGY

First-principles calculations were performed using the CASTEP module in Materials Studio, based on density functional theory (DFT). The exchange–correlation energy was treated using the Perdew–Burke–Ernzerhof (PBE) functional within the framework of the generalized gradient approximation (GGA) [26-27]. Norm-conserving pseudopotentials were employed to describe the electron–ion interactions, ensuring accurate treatment of core–valence effects. The valence electron configurations considered were $5s^25p^66s^1$, $5d^{10}6s^26p^3$ and $5s^25p^5$. A plane wave cut-off energy of 500 eV was used. The convergence thresholds were set at 10^{-5} eV for energy and 0.01 eV/Å for force. The structures of $Cs_3Bi_2I_9$, $Cs_3Bi_2Br_9$, and $Cs_3Bi_2Cl_9$ were fully relaxed during geometry optimization, for which the Brillouin zone was sampled using Gamma-centered k-point meshes of 4×4×4, 4×4×4, and 4×4×2, respectively [28-30]. Structural optimization was performed using the Broyden–Fletcher–Goldfarb–Shanno (BFGS) minimization scheme until the convergence thresholds were satisfied: total energy change below 1.0×10^{-6} eV per atom, maximum force less than 0.01 eV/Å, [16] maximum displacement below 0.001 Å, and maximum stress not exceeding 0.02 GPa. The optimized lattice parameters were consistent with

previous reports, validating the reliability of the computational setup [31-32].

Electronic band structures were computed along high-symmetry directions in the hexagonal Brillouin zone (G → H) [33]. The total and partial density of states (DOS) were obtained from self-consistent field (SCF) calculations using relaxed geometry, with the Fermi level set to 0 eV as the reference energy. Optical properties were evaluated based on the complex dielectric function, $\varepsilon(\omega) = \varepsilon_1(\omega) + i\varepsilon_2(\omega)$, where $\varepsilon_2(\omega)$ was derived from interband transitions via momentum matrix elements, and $\varepsilon_1(\omega)$ was obtained using the Kramers–Kronig relation. The absorption coefficient, refractive index, and reflectivity spectra were subsequently calculated from these optical constants.

To assess the influence of external deformation, hydrostatic mechanical strain was applied to the optimized $Cs_3Bi_2X_9$ structure in the range of ±5 % [34]. All lattice constants (a, b, and c) were uniformly scaled by ±5 % from their equilibrium values to simulate isotropic compression and expansion. After each strain application, the atomic positions were fully relaxed to obtain the minimum energy configuration. The corresponding band structures and electronic properties were then recalculated to examine the effect of strain on the band gap and overall electronic behaviour [35]. The ±5 % strain range was selected as it represents a moderate level of deformation that remains within the elastic limits of most inorganic perovskites. Strains beyond this threshold often result in structural instability or cause unrealistic bond distortions in DFT simulations. Prior theoretical studies on related halide perovskites, such as $CsPbX_3$ and Bi-based perovskites, have also employed strain magnitudes of up to 5 % to investigate its effects on electronic and optical properties without inducing structural phase transitions or mechanical failure [34]. Therefore, restricting the applied strain to ±5 % ensures a reliable and physically meaningful window for exploring the impact of hydrostatic deformation on $Cs_3Bi_2X_9$.

RESULTS AND DISCUSSION

Structural Properties

Figure 1 illustrates the optimized crystal structures of $Cs_3Bi_2I_9$, $Cs_3Bi_2Br_9$ and $Cs_3Bi_2Cl_9$. As shown in Figure 1(a), $Cs_3Bi_2I_9$ adopted a trigonal crystal structure composed of isolated face-sharing $[BiI_6]$ octahedra forming discrete $[Bi_2I_9]^{3-}$ bioctahedral units arranged within a hexagonal unit cell. Caesium ions occupy the interstitial sites between these clusters, resulting in a zero-dimensional perovskite-like framework. This structural motif is characteristic of bismuth-based halide perovskites and is known to contribute to their enhanced structural stability.

The optimized $Cs_3Bi_2I_9$ structure crystallized in the $P6_3/mmc$ space group, consistent with experimentally reported trigonal symmetry. In this configuration, the lattice parameter *a* corresponds to the in-plane hexagonal lattice constant, while *c* represents the stacking direction perpendicular to the bioctahedral layers. Experimentally, $Cs_3Bi_2I_9$ typically exhibits lattice parameters of $a = b \approx 8.40$ Å and $c \approx 21.18$ Å [31, 36]. In the present study, the optimized lattice constants obtained were $a = b = 8.66(2)$ Å and $c = 22.36(3)$ Å, where the values in parentheses represent the estimated uncertainty in the last digit arising from geometry convergence. The close agreement between calculated and reported values confirms the reliability of the adopted computational methodology [37].

Figures 1(b) and 1(c) present the fully optimized structures of $Cs_3Bi_2Br_9$ and $Cs_3Bi_2Cl_9$, respectively. Both compounds retained the characteristic $[Bi_2X_9]^{3-}$ bioctahedral framework but crystallized in different trigonal space groups, namely P-3m1 for $Cs_3Bi_2Br_9$ and $P\bar{3}21$ for $Cs_3Bi_2Cl_9$. These differences in space group symmetry originate from the progressive reduction in halide ionic radius ($I^- > Br^- > Cl^-$), which induces variations in Bi–X bond lengths, octahedral tilting, and interlayer packing. As the halide size decreases, the crystal structure becomes more compact, leading to symmetry lowering and structural rearrangement.

A systematic contraction of the lattice parameters was observed across the halide series. The optimized lattice constants decreased from $Cs_3Bi_2I_9$ to $Cs_3Bi_2Br_9$ ($a = b = 7.99(2)$ Å, $c = 20.13(3)$ Å) and further to $Cs_3Bi_2Cl_9$ ($a = b = 7.56(2)$ Å, $c = 18.92(3)$ Å), in excellent agreement with experimental and theoretical reports [38-40]. This trend reflects the reduced ionic size of Br^- and Cl^-, which promotes stronger Bi–X bonding and denser atomic packing.

A comparative summary of calculated and reported lattice parameters for $Cs_3Bi_2X_9$ (X = I, Br, Cl) is presented in Table 1, demonstrating the strong consistency between the present results and existing literature. These findings establish a robust structural foundation for the subsequent analysis of the electronic, optical and strain-dependent properties of $Cs_3Bi_2X_9$ compounds.

Table 1. Comparison of Reported Lattice Parameters for $Cs_3Bi_2X_9$.

	a (Å)	b(Å)	c(Å)	Ref
$Cs_3Bi_2I_9$ - P63/mcc	8.66	8.66	22.36	[a] Current
	8.40	8.40	21.18	[a] [41]
	8.33	8.33	21.32	[b] [42]
	8.39	8.39	21.20	[b] [43]
	8.40	8.40	21.18	[a] [30]
	8.40	8.40	21.18	[a] [35]
	8.66	8.66	22.36	[b] [36]
$Cs_3Bi_2Br_9$ - P-3m1	7.99	7.99	20.13	[a] Current
	8.04	8.04	9.85	[b] [37]
$Cs_3Bi_2Cl_9$ - P3$_2$1	7.56	7.56	18.97	[a] Current
	7.68	7.68	9.46	[b] [38]
	18.64	7.61	13.18	[b] [39]

[a] theoretical, [b] experiment,

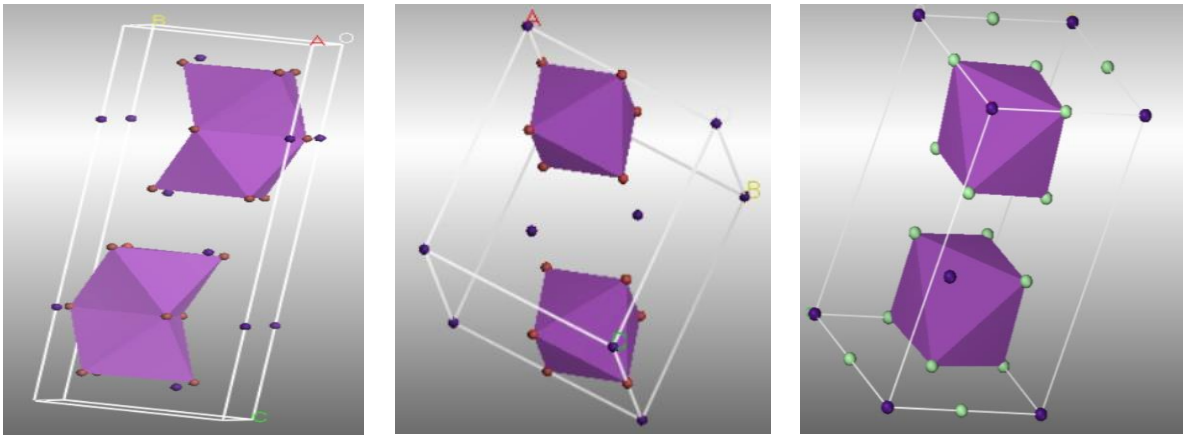

(a) (b) (c)

Figure 1. Optimized crystal structures of (a) $Cs_3Bi_2I_9$, (b) $Cs_3Bi_2Br_9$ and (c) $Cs_3Bi_2Cl_9$

Optical Properties

The optical absorption spectra of $Cs_3Bi_2I_9$, $Cs_3Bi_2Br_9$ and $Cs_3Bi_2Cl_9$ are illustrated in Figure 2. The optical absorption of $Cs_3Bi_2I_9$ appeared at around 630 nm, which corresponds to a computed band gap of 1.96 eV, confirming significant absorption in the visible range, a critical feature for photovoltaic performance. The spectrum exhibits multiple sharp absorption peaks at shorter wavelengths (below 300 nm), associated with strong electronic transitions between the valence and conduction bands. The high absorption coefficient values of nearly 200,000 cm^{-1} are characteristic of theoretical simulations, where idealized conditions exclude real-world limitations such as surface roughness, grain boundaries, or film thickness. These results suggest that $Cs_3Bi_2I_9$ possesses strong intrinsic optical absorption properties, making it a promising lead-free candidate for absorber layers in perovskite solar cells. Nonetheless, experimental verification using UV-Vis spectroscopy is recommended to validate these theoretical findings and assess performance under practical conditions.

The absorption spectrum of $Cs_3Bi_2Br_9$ in Figure 2(b) shows a sharp absorption edge in the visible region, with a strong absorption coefficient exceeding 2.0×10^5 cm^{-1} near the band edge. The steep decline beyond the onset indicates a direct band gap transition, while the negligible absorption in the longer wavelength region reflects the transparency of the material in the near-infrared range. This strong absorption near the band edge suggests that $Cs_3Bi_2Br_9$ can effectively harvest visible light, making it a promising candidate for lead-free perovskite solar cell applications.

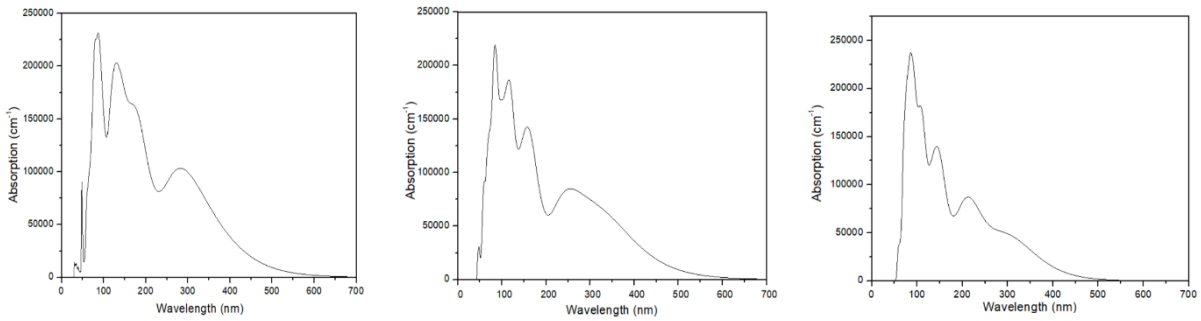

(a) (b) (c)

Figure 2. Simulated optical absorption spectra of (a) $Cs_3Bi_2I_9$, (b) $Cs_3Bi_2Br_9$ and (c) $Cs_3Bi_2Cl_9$ from CASTEP.

The absorption spectrum of $Cs_3Bi_2Cl_9$ in Figure 2(c) exhibits a sharp and intense absorption peak in the ultraviolet region, with a strong absorption coefficient exceeding 2.0×10^5 cm^{-1}, which rapidly decreased as the wavelength increased. The absorption edge is observed at shorter wavelengths compared to $Cs_3Bi_2I_9$ and $Cs_3Bi_2Br_9$, consistent with the wider band gap of the chloride-based compound. This indicates that $Cs_3Bi_2Cl_9$ primarily absorbed high-energy photons in the UV range, while exhibiting minimal absorption in the visible and near-infrared regions, which aligns with its electronic structure and potential applications in UV photodetection rather than visible-light photovoltaics.

Electronic Properties

Figure 3(a) illustrates the electronic band structure of $Cs_3Bi_2I_9$, computed using density functional theory (DFT) within the CASTEP module. The x-axis represents the wave vector along the high-symmetry points in the Brillouin zone, while the y-axis denotes the energy levels in electron volts (eV). To determine the band gap, the highest occupied electronic state in the valence band (valence band maximum, VBM) and the lowest unoccupied state in the conduction band (conduction band minimum, CBM) were examined. The energy difference between these two points represents the fundamental band gap of the material. From the computational results, the band gap of $Cs_3Bi_2I_9$ was found to be 1.96 eV, indicating strong electronic transitions and potential for high-energy photon absorption. This band gap value positions $Cs_3Bi_2I_9$ as an attractive material for optoelectronic applications, particularly in solar energy harvesting and photodetection. Materials with band gaps in this range have demonstrated promising photovoltaic performance, as they effectively absorb light in the visible spectrum while maintaining high open-circuit voltages, which is essential for efficient charge carrier extraction. The ability of $Cs_3Bi_2I_9$ to exhibit a stable electronic structure further enhances its appeal for lead-free perovskite solar cells, where long-term durability and non-toxicity are crucial factors [14].

Figure 3(b) shows the calculated band structure of $Cs_3Bi_2Br_9$. This material possesses an indirect band gap similar to $Cs_3Bi_2I_9$, with the valence band maximum (VBM) and conduction band minimum (CBM) occurring at different k-points. The computed band gap was 2.46 eV, wider than that of the iodide counterpart. The separation of band edges and flat dispersion near the band extrema suggest limited charge carrier mobility, a known limitation in bismuth-based halide perovskites. Although this material exhibits a wider band gap, such a property can be advantageous for future device applications, particularly in layered or heterojunction solar cell architectures, where materials with higher band gaps are often used to achieve larger open-circuit voltages (V_{oc}) and improved carrier separation.

Figure 3(c) shows the calculated band structure of $Cs_3Bi_2Cl_9$. As with $Cs_3Bi_2I_9$ and $Cs_3Bi_2Br_9$, this material exhibits an indirect band gap, with the valence band maximum (VBM) and conduction band minimum (CBM) occurring at different k-points. The computed band gap was 3.05 eV, the widest among the three halides, consistent with the stronger electronegativity and smaller ionic radius of Cl^-. The band dispersion around the VBM and CBM remained relatively flat, suggesting limited charge carrier mobility, which is a characteristic limitation of bismuth-based halide perovskites. However, the relatively large band gap of $Cs_3Bi_2Cl_9$ may be advantageous for applications requiring high optical transparency or as a potential top-layer material in tandem solar cell architectures, where wide-band gap absorbers are typically employed to enhance overall device efficiency and open-circuit voltage (V_{oc}).

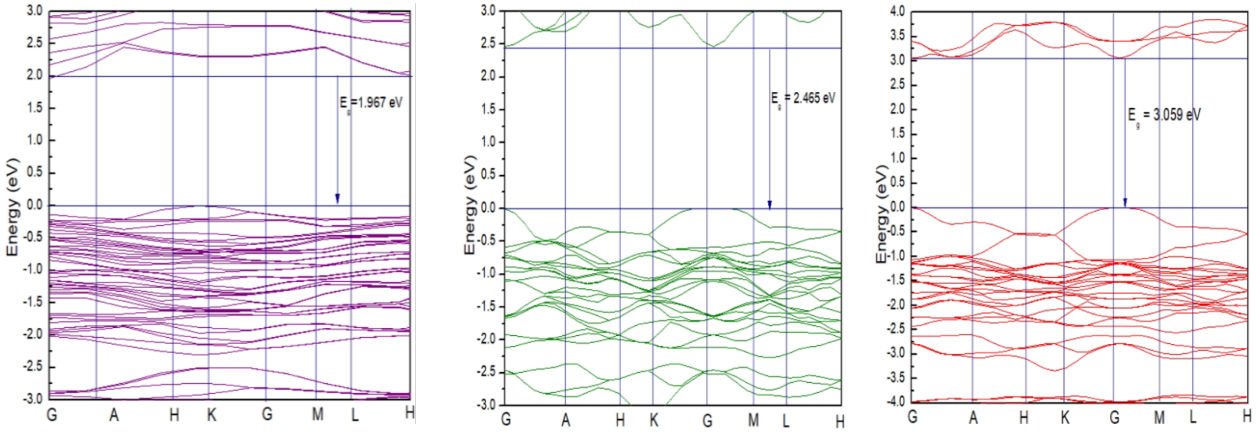

(a) (b) (c)

Figure 3. Electronic band structures of (a) $Cs_3Bi_2I_9$, (b) $Cs_3Bi_2Br_9$ and (c) $Cs_3Bi_2Cl_9$ from CASTEP.

In this study, the term "strong electronic transitions" refers to optical transitions with high transition probability between the valence band maximum (VBM) and conduction band minimum (CBM), as reflected by the large calculated absorption coefficients. From the projected density of states, the VBM of $Cs_3Bi_2X_9$ (X = I, Br, Cl) is predominantly composed of halide p orbitals, while the CBM is mainly derived from Bi 6p states. The strong orbital overlap between these states facilitates intense p–p transitions under photon excitation.

Among the three halide systems, $Cs_3Bi_2I_9$ exhibited the strongest optical response in the visible region, which can be attributed to the higher polarizability of iodide ions and a reduced band gap, leading to enhanced transition matrix elements. In contrast, substitution with Br and Cl resulted in stronger Bi-X bonding and increased electronic localization, shifting the absorption edge towards the ultraviolet region and reducing overall absorption intensity. This systematic trend highlights the critical role of halide chemistry in governing electronic transitions and optical strength in bismuth-based halide perovskites.

All $Cs_3Bi_2X_9$ compounds studied exhibited an indirect band gap, which generally implies reduced radiative recombination rates and lower charge carrier mobility compared to direct band gap materials. In photovoltaic applications, indirect band gaps may lead to reduced carrier collection efficiency due to phonon-assisted transitions being required for electron excitation and recombination.

However, despite this limitation, $Cs_3Bi_2X_9$ materials still demonstrate high absorption coefficients, indicating that strong light–matter interactions can partially compensate for the indirect nature of the band gap, particularly in sufficiently thick absorber layers. Additionally, the reduced radiative recombination associated with indirect band gaps may contribute to improved carrier lifetimes, which is beneficial for charge extraction in solar cell devices.

Importantly, the application of mechanical strain is shown to modify the band dispersion near the VBM and CBM, suggesting a possible route toward band structure engineering. Under strain, changes in Bi–X bond lengths and octahedral distortions alter orbital overlap, which may reduce the indirectness of the band gap or enhance transition probabilities. This strain-induced tunability provides an additional degree of freedom to optimize $Cs_3Bi_2X_9$ for optoelectronic and photovoltaic applications, despite its intrinsic indirect band gap character.

Strain-dependent Properties

The application of external strain is an effective approach to modulate the structural and electronic behaviour of halide perovskites, particularly when employed in thin-film or flexible device configurations. In this study, mechanical strain was simulated for $Cs_3Bi_2X_9$ (X = I, Br, Cl) by varying the lattice constants relative to their equilibrium values. The optimized lattice parameters at equilibrium were found to be a = 8.66 Å, b = 8.66 Å, c = 22.36 Å for $Cs_3Bi_2I_9$, a = b = 7.99 Å, c = 20.13 Å for $Cs_3Bi_2Br_9$, and a = b = 7.56 Å, c = 18.92 Å for $Cs_3Bi_2Cl_9$.

To investigate the effect of mechanical deformation, both tensile (+5 %) and compressive (−5 %) strains were applied by uniformly scaling all lattice parameters (a, b, and c) by ±5 % from their optimized equilibrium values [34]. This approach corresponds to hydrostatic strain, allowing the entire structure to expand or contract proportionally in all directions. After applying the strain, full structural relaxation of atomic positions was performed to ensure that each configuration reached its minimum energy state. The resulting strained lattice parameters are summarized in Table 2.

Table 2. Lattice parameters of $Cs_3Bi_2X_9$ (X = I, Br, Cl) under different strain conditions.

Strain (%)	Lattice parameter					
	$Cs_3Bi_2I_9$		$Cs_3Bi_2Br_9$		$Cs_3Bi_2Cl_9$	
	a = b (Å)	c (Å)	a = b (Å)	c (Å)	a = b (Å)	c (Å)
-5	8.23	21.24	7.59	19.13	7.19	17.97
0	8.66	22.36	7.99	20.13	7.56	18.92
5	9.09	23.48	8.39	21.14	7.94	19.87

Table 3. Band gaps of $Cs_3Bi_2X_9$ (X = I, Br, Cl) under strain.

Compound	Band gap (0 % strain)	Band gap (+5 % tensile)	Band gap (-5 % tensile)
$Cs_3Bi_2I_9$	1.96 eV	2.39 eV	2.37 eV
$Cs_3Bi_2Br_9$	2.46 eV	2.43 eV	2.20 eV
$Cs_3Bi_2Cl_9$	3.05 eV	3.00 eV	2.98 eV

The calculated band gaps under strain are presented in Table 3. For $Cs_3Bi_2I_9$, both tensile (+5 %) and compressive (–5 %) strain resulted in band gap widening, which can be attributed to distortions of the $[Bi_2I_9]^{3-}$ clusters that reduce orbital overlap at the valence band maximum, a mechanism consistent with strain-induced band alterations in related bismuth halide systems [15]. In contrast, $Cs_3Bi_2Br_9$ and $Cs_3Bi_2Cl_9$ exhibited band gap narrowing under compressive strain, as enhanced Bi–X orbital overlap in their stiffer lattices facilitates an upward shift of the valence band, consistent with prior strain-dependent DFT studies on halide perovskites [44]. These results demonstrate that strain engineering affects each halide differently: iodide is highly strain-sensitive but becomes less favourable for photovoltaic absorption under deformation, whereas bromide and chloride exhibit smaller yet potentially beneficial band gap reductions under compressive strain.

The results indicate that strain can effectively tune the electronic structure of $Cs_3Bi_2X_9$ compounds, with $Cs_3Bi_2I_9$ showing the strongest sensitivity to external deformation. The smaller band gap variations in $Cs_3Bi_2Br_9$ and $Cs_3Bi_2Cl_9$ are attributed to stronger Bi–X bonding and more rigid lattice frameworks. Importantly, the correlation between strain, band structure, and density of states (DOS) suggests that strain engineering may serve as a powerful tool to optimize the optoelectronic properties of $Cs_3Bi_2X_9$, potentially enhancing their performance in photovoltaic applications and enabling band-gap alignment for tandem solar cell designs.

CONCLUSION

In this study, the structural, electronic, optical, and strain-dependent properties of caesium bismuth halide perovskites $Cs_3Bi_2X_9$ (X = I, Br, Cl) were systematically investigated using first-principles calculations based on density functional theory (DFT). The optimized lattice parameters for all compositions showed good agreement with reported experimental and theoretical data, validating the reliability of the computational approach. The calculated band structures revealed that all compounds possessed indirect band gaps, which increased with decreasing halide ionic radius from I to Cl. $Cs_3Bi_2I_9$ exhibited a suitable band gap for visible-light absorption, whereas $Cs_3Bi_2Br_9$ and $Cs_3Bi_2Cl_9$ displayed wider band gaps, suggesting their potential for UV or tandem solar cell applications. Optical analysis further indicated strong absorption in the visible region for $Cs_3Bi_2I_9$ and higher transparency for $Cs_3Bi_2Cl_9$. Under biaxial strain (±5 %), $Cs_3Bi_2I_9$ demonstrated notable band gap tunability, highlighting its potential for band engineering through strain modulation, whereas $Cs_3Bi_2Br_9$ and $Cs_3Bi_2Cl_9$ exhibited comparatively smaller variations. Overall, these findings demonstrate that both halide substitution and strain engineering are effective strategies for tuning the optoelectronic response of $Cs_3Bi_2X_9$ perovskites, providing valuable insights for the development of stable, sustainable, and lead-free materials in next-generation photovoltaic and optoelectronic applications.

ACKNOWLEDGEMENTS

We would like to thank the National Defence University of Malaysia for the research grant UPNM/2025/GPPP/ST/1. We would also like to express our gratitude to CADRE in PAP, UPNM for their support and for providing research facilities to conduct this research.

REFERENCES

1. Kim, J. Y., Lee, J. W., Jung, H. S., Shin, H. & Park, N. G. (2020) High-Efficiency Perovskite Solar Cells. *Chem. Rev.*, **120**, 7867–7918.

2. Zhang, X. (2024) High-Efficiency Perovskite Solar Cells: Progress and Prospects. *E3S Web. Conf.*, **553**, 8–11.

3. Cao, F., Bian, L. & Li, L. (2024) Perovskite solar cells with high-efficiency exceeding 25%: A review. *Energy Mater, Devices*, **2**.

4. Raju, T. D. (2025) Advancements in perovskites for solar cell commercialization: A review. *Adv. Powder Mater,* **4**, 100275.

5. Roß, M. (2021) Co-Evaporated Formamidinium Lead Iodide Based Perovskites with 1000 h Constant Stability for Fully Textured Monolithic Perovskite/Silicon Tandem Solar Cells. *Adv. Energy Mater*, **11**.

6. Benmessaoud, I. R. (2016) Health hazards of methylammonium lead iodide based perovskites: Cytotoxicity studies. *Toxicol. Res. (Camb)*, **5**, 407–419.

7. Awang, H., Hezam, A., Peppel, T. & Strunk, J. (2024) Enhancing the Photocatalytic Activity of Halide Perovskite Cesium Bismuth Bromide/ Hydrogen Titanate Heterostructures for Benzyl Alcohol Oxidation. *Nanomaterials*, **14**.

8. Nelson, R. D. (2018) Synthesis and optical properties of ordered-vacancy perovskite cesium bismuth halide nanocrystals. *Chem. Commun.*, **54**, 3640–3643.

9. López-Fernández, I. (2024) Lead-Free Halide Perovskite Materials and Optoelectronic Devices: Progress and Prospective. *Adv. Funct. Mater*, **34**.

10. Adjogri Shadrack, J., Meyer Edson, L. (2020) A Review on Lead-Free Hybrid Halide Perovskites as Light Absorbers for Photovoltaic Applications Based on Their Structural, Optical, and Morphological Properties. *Molecules*, **25**, 1–40.

11. Gao, P., Grätzel, M. & Nazeeruddin, M. K. (2014) Organohalide lead perovskites for photovoltaic applications. *Energy Environ. Sci.*, **7**, 2448–2463.

12. Berhe, T. A., Su, W. N. & Hwang, B. J. (2024) Halide Perovskites' Multifunctional Properties: Coordination Engineering, Coordination Chemistry, Electronic Interactions and Energy Applications beyond Photovoltaics. *Inorganics*, **12**.

13. Magdalin, A. E. (2023) Development of lead-free perovskite solar cells: Opportunities, challenges, and future technologies. *Results Eng.*, **20**, 101438.

14. Peng, X. (2025) Halide Perovskite Nanostructures: Processing Methods and Optoelectronics Applications. *NPJ Nanophotonics*, **2**, 42.

15. Yang, B. (2022) Strain effects on halide perovskite solar cells. *Chem. Soc. Rev.*, **51**, 7509–7530.

16. Xiang, G. (2021) Dimension-dependent bandgap narrowing and metallization in lead-free halide perovskite Cs3Bi2X9 (X = I, Br, and Cl) under high pressure. *Nanomaterials*, **11**.

17. Jakubas, R., Bator, G. & Mróz, J. (1995) Dielectric and Pyroelectric Studies on [N(CH 3) 4] 3 Bi 2 X 9 (X = Cl, Br). *Acta Phys. Pol. A*, **87**, 663–669.

18. Photodetector, M. L. P. (2022) Potassium Iodide-Modified Lead-Free Cs3Bi2I9 Perovskites for Enhanced High-Efficiency Solar Cells. *Nanomaterials*, **12**, 3751.

19. Kumar, S. G., Reddy, T. S. T., Suraj, N. & Prashanth, C. R. (2024) Investigating the Performance of A3B2X9 (Cs3Bi2I9) Based Perovskite Photovoltaic Tandem Structure with Crystalline Silicon (c-Si). *SSRG Int. J. Electr. Electron. Eng.*, **11**, 12–21.

20. Luo, T. & Wei, J. (2020) First principles study of electronic and optical properties of inorganic and lead-free perovskite: Cs3Bi2X9 (X: Cl, Br, I). *Mater. Chem. Phys.*, **253**, 123374.

21. Long, Y., Zhang, H. & Cheng, X. (2022) Stability, electronic structure, and optical properties of lead-free perovskite monolayer Cs3B 2X 9(B = Sb, Bi; X = Cl, Br, I) and bilayer vertical hetero-structure Cs3B 2X 9/Cs3X 9(B,B′ = Sb, Bi; X = Cl, Br, I). *Chinese Phys. B*, **31**.

22. Yang, B. (2017) Lead-Free, Air-Stable All-Inorganic Cesium Bismuth Halide Perovskite Nanocrystals. *Angew. Chemie - Int. Ed.*, **56**, 12471–12475.

23. Lin, C. H. (2024) Density-Functional Theory Studies on Photocatalysis and Photoelectro-catalysis: Challenges and Opportunities. *Sol. RRL,* **8**.

24. Rizwan, M. (2019) Structural, electronic and optical properties of copper-doped SrTiO3 perovskite: A DFT study. *Phys. B Condens. Matter,* **552**, 52–57.

25. Liang, H. (2023) Strain Effects on Flexible Perovskite Solar Cells. *Adv. Sci*., **10**, 1–30.

26. Ghaleb, A. M. & Ahmed, A. Q. (2022) Structural, electronic, and optical properties of sphalerite ZnS compounds calculated using density functional theory (DFT). *Chalcogenide Lett.*, **19**, 309–318.

27. Arif, H. (2023) CASTEP study for mapping phase stability, and optical parameters of halide perovskite CsSiBr3 for photovoltaic and solar cell applications. *Inorg. Chem. Commun*, **150**, 110474.

28. Zhang, L. (2018) Pressure-Induced Emission Enhancement, Band-Gap Narrowing, and Metallization of Halide Perovskite Cs3Bi2I9. *Angew. Chemie - Int. Ed.*, **57**, 11213–11217.

29. Usman Ghani, M. (2023) CASTEP investigation of structural, electronic, and optical properties of halide perovskites RbXCl3 (X = Ge, Sn, Pb) for solar cell applications. *Inorg. Chem. Commun*, **155**.

30. Christopoulos, S. R. G., Papadopoulou, K. A., Konios, A. & Parfitt, D. (2022) DIMS: A tool for setting up defects and impurities CASTEP calculations. *Comput. Mater. Sci.*, **202**, 110976.

31. Tailor, N. K. & Satapathi, S. (2020) Structural Disorder and Spin Dynamics Study in Millimeter-Sized All-Inorganic Lead-Free Cesium Bismuth Halide Perovskite Single Crystals. *ACS Appl. Energy Mater,* **3**, 11732–11740.

32. Pancielejko, A. (2024) Rational designing of TiO2-X@Cs3Bi2X9 nanocomposite for boosted hydrogen evolution. *Catal. Today*, **432**.

33. Islam, J. & Hossain, A. K. M. A. (2020) Semi-conducting to metallic transition with outstanding optoelectronic properties of CsSnCl3 perovskite under pressure. *Sci. Rep.*, **10**, 1–11.

34. Husin, R., Badrudin, F. W., Taib, M. F. M. & Yahya, M. Z. A. (2019) Effects of strain on electronic and optical properties of LiNbO3: A first principles study. *Mater. Res. Express*, **6**.

35. Wang, X., Bi, G., Ali, N., Chen, Y. & Wu, H. (2021) Theoretical study of the strain influence on lead-free bismuth-based halide perovskites. *J. Mater. Sci.*, **56**, 11377–11385.

36. Arakcheeva, A. V., Chapuis, G. & Meyer, M. (2001) The LT phase of Cs3Bi2I9. *Zeitschrift fur Krist*, **216**, 199–205.

37. Wen, H. (2024) Structural, Electronic, and Optical Properties of Halide Perovskite Cs3Bi2I9: Density Functional Calculations. *Russ. J. Phys. Chem. A*, **98**, 3144–3151.

38. Valastro, S. (2024) Temperature-Dependent Excitonic Band Gap in Lead-Free Bismuth Halide Low-Dimensional Perovskite Single Crystals. *Adv. Opt. Mater*, **12**, 1–10.

39. Morgan, E. E., Mao, L., Teicher, S. M. L., Wu, G. & Seshadri, R. (2020) Tunable Perovskite-Derived Bismuth Halides: Cs3Bi2(Cl1- xIx)9. *Inorg. Chem.*, **59**, 3387–3393.

40. Ghosh, B. (2019) Bismuth halide semiconductors: a combined theoretical and experimental approach for photovoltaics, 1–174.

41. Kamalarasan, V., Santhosh Kumar, B., Mukilraj, T. & Venkateswaran, C. (2020) Optical property and thermal stability studies on Cs3Bi2I9 perovskite quantum dots for photovoltaic application. *AIP Conf. Proc.*, **2265**.

42. Gu, J. (2018) Bandgap engineering of a lead-free defect perovskite Cs3Bi2I9 through trivalent doping of Ru3+. *RSC Adv.*, **8**, 25802–25807.

43. Zhang, Y. (2020) Nucleation-controlled growth of superior lead-free perovskite Cs3Bi2I9 single-crystals for high-performance X-ray detection. *Nat. Commun.*, **11**, 2304.

44. Haque, M. M., Amanullah, M., Mia, M. R. & Islam, M. R. (2024) Strain effect on the electronic and optical characteristics of FAGeX3 (X=Cl, Br, and I) perovskite materials: DFT analysis. *Heliyon*, **10**, e39799.